High-Bandwidth Harmonics-Suppressed Dynamic Phase-Synchronized Adaptive Notch Observer for High-Frequency Injection Based Sensorless Drive

Guangyu Pu, *Student Member, IEEE*, Hanlin Zhan, *Member, IEEE*, Wenzhi Liu, Hui Yang, *Senior Member, IEEE*, Lei Yang, and Dianguo Xu, *Fellow, IEEE*

***Abstract*—In high-frequency injection-based saliency tracking, harmonic errors arise from nonidealities in interior permanent magnet synchronous motor and inverter. Conventionally, achieving both high-bandwidth observation and reduced low-order harmonics presents an inherent tradeoff. Adaptive notch filter (ANF), featuring harmonic suppression characteristic without affecting the target signal, is gaining increasing attention. In this article, the saliency tracking bandwidth-constrained divergence phenomenon in conventional ANF-based harmonic suppression is first revealed. Due to the inherent closed-loop nature in saliency tracking, there is inevitable phase misalignment between detection and compensation, which could lead to high risk of divergence in harmonic suppression, especially in low-speed and high bandwidth observation. Subsequently, a novel dynamic phase-synchronized adaptive notch observer is proposed, which has the ability to counteract the closed-loop effect. The convergence boundary is expanded and full-order harmonics can be suppressed under high-bandwidth observation at low-speed. The convergence boundary is analytically proven and the enhancements of the proposed harmonic suppression method are verified with experiments.**

***Index Terms*—Dynamic phase-synchronized adaptive notch observer (DPS-ANO), harmonics suppression, high-frequency (HF) injection, high-bandwidth, interior permanent magnet synchronous motor (IPMSM).**

Received 8 July 2025; revised 25 September 2025; accepted 27 October 2025. Date of publication 31 October 2025; date of current version 19 January 2026. This work was supported in part by the National Key R&D Program of China under Grant 2022YFB3403202, in part by Guangdong Basic and Applied Basic Research Foundation under Grant 2025B1515020063, in part by Shenzhen Science and Technology Program under Grant RCYX20221008092928073, and in part by State Key Laboratory of High-end Heavy-load Robots Open Fund Project under Grant HHR2024010102. Recommended for publication by Associate Editor A. Dekka. *(Corresponding author: Hanlin Zhan.)*

Guangyu Pu, Hanlin Zhan, and Wenzhi Liu are with the Department of Robotics and Advanced Manufacturing, Harbin Institute of Technology Shenzhen, Shenzhen 518055, China (e-mail: guangyupu@stu.hit.edu.cn; zhanhanlin@hit.edu.cn; wenzhiliu@stu.hit.edu.cn).

Hui Yang is with the College of Automation Engineering, Nanjing University of Aeronautics and Astronautics, Nanjing 211106, China (e-mail: yang.hui@nuaa.edu.cn).

Lei Yang is with the State Key Laboratory of High-end Heavy-load Robots, Foshan 528311, China (e-mail: yanglei34@midea.com).

Dianguo Xu is with the School of Electrical Engineering and Automation, Harbin Institute of Technology, Harbin 150001, China (e-mail: xudiang@hit.edu.cn).

Color versions of one or more figures in this article are available at https://doi.org/10.1109/TPEL.2025.3627874.

Digital Object Identifier 10.1109/TPEL.2025.3627874

I. Introduction

INTERIOR permanent magnet synchronous motor (IPMSM) has been widely applied in various applications for its high efficiency and high power density. Accurate rotor position sensing is essential for high-performance control, whereas the additional position sensors introduce both cost penalties and reliability concerns. Hence, sensorless methods for IPMSM have been widely investigated. In middle and high speed ranges, prevailed performance can be achieved via the back-EMF-based sensorless methods [1], [2]. While in low-speed and standstill, rotor saliency tracking methods based on high-frequency (HF) injection are widely adopted [3], [4], [5], [6]. However, the nonidealities in IPMSM and inverter could produce remarkable harmonics in estimated position [7], [8], [9], [10], [11]. Reigosa et al. [7] indicate that the second-order harmonics will be produced from the asymmetrical parameters in machine parameters. Besides, the sixth-order harmonics exists due to the inverter nonlinearity [8], [9]. For HF injection (HFI)-based sensorless methods, the sixth-order harmonics also comes from the spatial harmonics of inductances [10]. Additionally, the third-order harmonics will be produced by voltage distortion when switching frequency injection is applied [11].

In back-EMF-based position observation, the compensation-based methods [12], [13] and the filtering-based methods [14], [15], [16], [17] have been widely applied to suppress the estimation harmonics. In [12], the enhanced Luenberger-style back-EMF tracking observer is proposed coping with the effect of inverter nonlinearity. Ye and Yao [13] propose an enhanced SMO with fuzzy logic controller self-adjusted shape coefficient, where the harmonics produced from current errors are analyzed and compensated. Additionally, filtering-based methods have attracted increasing attention, where the integration of adaptive transfer function is widely investigated, [14], [15], [16], [17]. The double quasi-proportional resonant (QPR) controllers are embedded in phase-locked loop (PLL) in [14], where the position harmonics can be separated and suppressed. Xu et al. [15] adopt the second-order generalized integrator (SOGI) structure, which is characterized with adaptive harmonics attenuation capability. Wu et al. [16] integrate a bilinear recursive least squares adaptive filter into sliding-mode observer (SMO)-based sensorless method and suppresses the dominant harmonic components. In [17], a notch filter based on the adaptive transfer

function structure is proposed and applied in the back-EMF-based method, where the enhanced robustness is achieved.

The adaptive notch filter (ANF) adaptively extracts harmonic features and suppresses harmonic errors while preserving target signal integrity, making it increasingly prevalent in recent studies [18], [19], [20]. Besides, the ANF has been applied to suppress the harmonics in the estimated orthogonal back-EMFs [21], [22], [23]. In [21], the ANF adaptively detects and compensates the fifth-order and seventh-order harmonics in estimated back-EMFs induced by inverter nonlinearity. In [22], the orthogonal master-slave ANF is adopted, achieving harmonics suppression and fast response concurrently in back-EMF-based sensorless methods. An amplitude-ANF is adopted in [23], which is utilized in a low-speed back-EMF-based sensorless strategy. Compared with compensation-based methods and filtering-based methods, the back-EMF-based methods utilizing ANF show the advantages of universality, effective low-order harmonic suppression ability and high-bandwidth position observation performance in low-speed. However, in saliency tracking-based sensorless method, the orthogonal sinusoidal signals are naturally absent. Therefore, the ANF cannot be adopted in saliency tracking directly as in back-EMF-based methods.

For HFI-based sensorless methods, the existing harmonic suppression methods can be mainly divided into machine design-based methods [24], [25], compensation-based methods [26], [27] and filtering-based method [28], [29], [30], [31]. Wang et al. [24] and Bianchi and Bolognani [25] alleviate the non-ideal saliency characteristics by adding saliency modulation rotor and optimizing the rotor geometry, respectively. Raute et al. [26] compensate the nonlinearities of the inverter and reduces the harmonics induced from the varying power devices resistance. An online harmonic compensation strategy is realized in [27] by utilizing the dual frequency injection. The filtering-based methods in [28] and [29] utilize the adaptive SOGI and transformation-based filter to diminish the harmonics, respectively. In [30] and [31], the QPR and Fourier iterative learning control (ILC) are, respectively, applied, suppressing the harmonics by feeding the estimated speed back. Whereas, the effective full-order harmonic (across all dominant harmonic orders) suppression is unprocurable in existing methods, which are neither limited to suppressing certain specific harmonics or poor in low-order harmonic rejection. Additionally, ANF is integrated in the position observer in HFI-based sensorless method in [32]. However, the inherent closed-loop nature of saliency tracking is not considered, which significantly limits the position observation performance.

However, the additional filtering loop or estimated speed feedback in saliency tracking will inevitably influence the position estimation process and reduce the observation bandwidth. Besides, the inherent closed-loop nature of saliency tracking is rarely considered in existing harmonic suppression methods, which leads to the ineffective suppression of low-order harmonics in saliency tracking in low-speed. The main contributions of the article can be summarized as follows:

1) It is first revealed that the previously overlooked inherent closed-loop nature in tracking observer inevitably leads to the degraded performance and even divergence in low-order harmonics suppression. Additionally, the convergence boundary is proposed and proven with both theoretical analysis and experimental results.
2) To solve the divergence problem produced by inherent closed-loop nature in conventional ANF, A novel dynamic phase-synchronized adaptive notch observer (DPS-ANO) is proposed, which counteracts the closed-loop effect and expands the convergence boundary, realizing full-order harmonic suppression and high-bandwidth position observation concurrently in HFI-based sensorless method.
3) An exhaustive analysis and comprehensive experimental comparisons of different harmonic suppression methods are conducted, which demonstrates the enhancement of the proposed DPS-ANO in harmonics suppression, target signal tracking and computational complexity for the machines with inductance saliency under low-speed high-bandwidth observation.

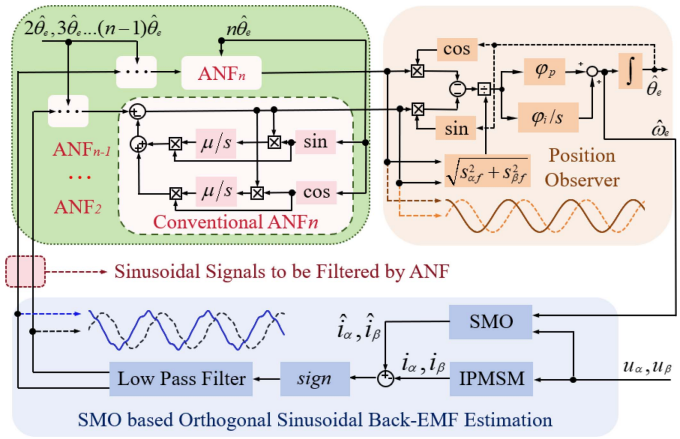

Fig. 1. Conventional ANF structure and its application in estimated orthogonal sinusoidal back-EMFs harmonics suppression.

This rest of this article is organized as follows. Section II introduces the ANF application in suppressing the harmonics of estimated back-EMFs. In Section III, the convergence boundary of conventional adaptive notch observer (ANO) considering the inherent closed-loop nature is first revealed. Section IV proposes the DPS-ANO, which solves the divergence problem produced by inherent closed-loop nature and realizes the full-order harmonic suppression under high-bandwidth observation concurrently. The proposed convergence boundary of conventional ANO and the enhancement of DPS-ANO are validated with experiments in Section V. Finally, Section VI concludes this article.

II. ANF Application in Suppressing Harmonics of Estimated Orthogonal Back-EMFs

The orthogonal back-EMFs can be estimated from the mathematic model of IPMSM. For instance, the SMO-based method, as shown in Fig. 1, obtains the back-EMFs based on voltage command (u_α, u_β) and sampled current (i_α, i_β). The state equation

of machine current can be written as

$$p\begin{bmatrix} i_\alpha \\ i_\beta \end{bmatrix} = \frac{1}{L_d}\left(\begin{bmatrix} -R_s & \omega_e(L_q - L_d) \\ \omega_e(L_d - L_q) & -R_s \end{bmatrix}\begin{bmatrix} i_\alpha \\ i_\beta \end{bmatrix} + \begin{bmatrix} u_\alpha - e_\alpha \\ u_\alpha - e_\beta \end{bmatrix}\right) \tag{1}$$

where L_d and L_q are the d-axis and q-axis inductances. R_s is the stator resistance. ω_e is rotor speed. p is differential operator. e_α and e_β are the extended back-EMF, defined as

$$\begin{bmatrix} e_\alpha \\ e_\beta \end{bmatrix} = [(L_d - L_q)(\omega_e i_d - p i_q) + \omega_e \psi_f]\begin{bmatrix} -\sin\theta_e \\ \cos\theta_e \end{bmatrix} \tag{2}$$

where i_d and i_q are the current in rotor synchronous reference frame (RRF). ψ_f is the flux linkage of permanent magnet (PM). θ_e is the rotor position. The SMO model is established as

$$p\begin{bmatrix} \hat{i}_\alpha \\ \hat{i}_\beta \end{bmatrix} = \frac{1}{L_d}\left(\begin{bmatrix} -R_s & \hat{\omega}_e(L_q - L_d) \\ \hat{\omega}_e(L_d - L_q) & -R_s \end{bmatrix}\begin{bmatrix} \hat{i}_\alpha \\ \hat{i}_\beta \end{bmatrix} + \begin{bmatrix} u_\alpha - v_\alpha \\ u_\alpha - v_\beta \end{bmatrix}\right) \tag{3}$$

where $\hat{i}_\alpha$ and $\hat{i}_\beta$ are the estimated current in SMO model. $\hat{\omega}_e$ is the estimated speed. v_α and v_β are the sliding-mode control rate, defined as

$$\begin{bmatrix} v_\alpha \\ v_\beta \end{bmatrix} = \begin{bmatrix} k \cdot \text{sign}(\hat{i}_\alpha - i_\alpha) \\ k \cdot \text{sign}(\hat{i}_\beta - i_\beta) \end{bmatrix} \tag{4}$$

where sign(x) returns +1 when $x>0$ and returns -1 when $x<0$. k is the sliding-mode gain. Hence, the filtered value of sliding-mode rate z_α and z_β, the orthogonal sinusoidal back-EMFs that contain both the position information and harmonics, can be expressed as follows

$$\begin{bmatrix} z_\alpha \\ z_\beta \end{bmatrix} = \text{LPF}\left(\begin{bmatrix} v_\alpha \\ v_\beta \end{bmatrix}\right) = \begin{bmatrix} e_\alpha \\ e_\beta \end{bmatrix} + \sum_{i=2,3\ldots}\begin{bmatrix} v_{\alpha ci}\cos i\theta_e + v_{\alpha si}\sin i\theta_e \\ v_{\beta ci}\cos i\theta_e + v_{\beta si}\sin i\theta_e \end{bmatrix} \tag{5}$$

where i stands for the ith-order harmonic.

$z_{\alpha f}$ and $z_{\beta f}$ containing null harmonic can be obtained from z_α and z_β via ANF as shown in Fig. 1. Where ANF$_n$ is for n^{th}-order harmonic suppression. The suppression can be realized as

$$\begin{bmatrix} z_{\alpha f} \\ z_{\beta f} \end{bmatrix} = \begin{bmatrix} z_\alpha \\ z_\beta \end{bmatrix} - \sum_{i=2,3\ldots}\begin{bmatrix} \hat{v}_{\alpha ci}\cos i\theta_e + \hat{v}_{\alpha si}\sin i\theta_e \\ \hat{v}_{\beta ci}\cos i\theta_e + \hat{v}_{\beta si}\sin i\theta_e \end{bmatrix} \tag{6}$$

where $\hat{v}_{\alpha si}$, $\hat{v}_{\alpha ci}$ and $\hat{v}_{\beta si}$, $\hat{v}_{\beta ci}$ are the estimated harmonic amplitude values, which can be obtained adaptively as

$$\begin{bmatrix} \hat{v}_{\alpha ci} \\ \hat{v}_{\alpha si} \end{bmatrix} = \int\left(\begin{bmatrix} \mu z_{\alpha f}\cos(i\hat{\theta}_e) \\ \mu z_{\alpha f}\sin(i\hat{\theta}_e) \end{bmatrix}\right)dt \tag{7}$$

$$\begin{bmatrix} \hat{v}_{\beta ci} \\ \hat{v}_{\beta si} \end{bmatrix} = \int\left(\begin{bmatrix} \mu z_{\beta f}\cos(i\hat{\theta}_e) \\ \mu z_{\beta f}\sin(i\hat{\theta}_e) \end{bmatrix}\right)dt \tag{8}$$

where μ denotes the adaptation gain ($\mu > 0$), and $\hat{\theta}_e$ represents the estimated rotor position generated by a quadrature PLL

$$\hat{\theta}_e = \int(\hat{\omega}_e)dt = \int[\varphi_p\varepsilon + \varphi_i\int(\varepsilon)dt]dt \tag{9}$$

where φ_p and φ_i are the parameters of PLL, ε is the estimation error signal, which are calculated as

$$\varphi_p = 2\xi\omega_n \tag{10}$$

$$\varphi_i = {\omega_n}^2 \tag{11}$$

$$\varepsilon = \frac{1}{\sqrt{{z_{\alpha f}}^2 + {z_{\beta f}}^2}}(z_{\beta f}\cos\hat{\theta}_e - z_{\alpha f}\sin\hat{\theta}_e) \tag{12}$$

where ξ and ω_n are the damping ratio and bandwidth of the PLL, respectively.

Consequently, harmonics present in the orthogonal back-EMF components z_α and z_β are adaptively suppressed by the proposed method, which preserves the integrity of position information and enhances estimation accuracy.

III. Harmonics-Suppressed ANO and Bandwidth Constrained Convergence Boundary

The orthogonal sinusoidal signals, while filtered by ANF in back-EMF-based method, are absent in saliency tracking. In this section, the ANF is cascaded into the saliency tracking observer, where the bandwidth-constrained divergence due to inherent closed-loop nature is firstly revealed and deduced analytically. It is indicated that, under high-bandwidth observation, the low-order harmonics suffer from high risk of divergence in low-speed.

A. ANO-Based Harmonics Suppression for HFI-Based Method

The ideal HF model of IPMSM in RRF can be written as

$$\begin{bmatrix} u^r_{dh} \\ u^r_{qh} \end{bmatrix} = \begin{bmatrix} pL_d & 0 \\ 0 & pL_q \end{bmatrix}\begin{bmatrix} i^r_{dh} \\ i^r_{qh} \end{bmatrix} \tag{13}$$

where u^r_{dh}, u^r_{qh} and i^r_{dh}, i^r_{qh} are the d- and q-axis HF voltage and current signals in RRF. Hence, in estimated rotor synchronous reference frame (ERRF), the HF model can be deduced as

$$\begin{bmatrix} u^{\hat{r}}_{dh} \\ u^{\hat{r}}_{qh} \end{bmatrix} = T(\theta_{err})\begin{bmatrix} pL_d & 0 \\ 0 & pL_q \end{bmatrix}T(-\theta_{err})\begin{bmatrix} i^{\hat{r}}_{dh} \\ i^{\hat{r}}_{qh} \end{bmatrix} \tag{14}$$

where $u^{\hat{r}}_{dh}$, $u^{\hat{r}}_{qh}$ and $i^{\hat{r}}_{dh}$, $i^{\hat{r}}_{qh}$ are the HF voltage and current signals in ERRF. θ_{err} equals to $\hat{\theta}_e - \theta_e$ and $\hat{\theta}_e$ is the angle of ERRF. The transformation matrix $T(\theta_{err})$ can be defined as

$$T(\theta_{err}) = \begin{bmatrix} \cos\theta_{\text{err}} & \sin\theta_{\text{err}} \\ -\sin\theta_{\text{err}} & \cos\theta_{\text{err}} \end{bmatrix}. \tag{15}$$

Hence, the HF current can be expressed as

$$\begin{bmatrix} i^{\hat{r}}_{dh} \\ i^{\hat{r}}_{qh} \end{bmatrix} = p^{-1}\begin{bmatrix} B_{dd}(\theta_{\text{err}}) & B_{dq}(\theta_{\text{err}}) \\ B_{qd}(\theta_{\text{err}}) & B_{qq}(\theta_{\text{err}}) \end{bmatrix}\begin{bmatrix} u^{\hat{r}}_{dh} \\ u^{\hat{r}}_{qh} \end{bmatrix} \tag{16}$$

where $B_{dd}(\theta_{\text{err}})$, $B_{dq}(\theta_{\text{err}})$, $B_{qd}(\theta_{\text{err}})$ and $B_{qq}(\theta_{\text{err}})$can be represented as

$$B_{dd}(\theta_{\text{err}}) = \frac{L_q \cos^2\theta_{\text{err}} + L_d \sin^2\theta_{\text{err}}}{L_d L_q} \tag{17}$$

$$B_{qq}(\theta_{\text{err}}) = \frac{L_d \cos^2\theta_{\text{err}} + L_q \sin^2\theta_{\text{err}}}{L_d L_q} \tag{18}$$

$$B_{qd}(\theta_{\text{err}}) = B_{dq}(\theta_{\text{err}}) = -\frac{\Delta L}{L_d L_q}\sin(2\theta_{\text{err}}) \tag{19}$$

where ΔL equals to (L_q-L_d)/2. In HFI, square-wave voltage signal injection is commonly employed to enhance observation bandwidth. The HF voltage signal can be expressed as

$$\begin{bmatrix} u^{\hat{r}}_{dh} \\ u^{\hat{r}}_{qh} \end{bmatrix} = \begin{bmatrix} V_{\text{inj}} \cdot \text{clk}[k] \\ 0 \end{bmatrix} \tag{20}$$

where V_{inj} is the injected voltage amplitude and clk$[k]$ is defined as

$$\text{clk}[k] = (-1)^k, k = 1, 2, 3 \ldots \tag{21}$$

by substituting (20) into (16), the variation of HF current $\Delta i^{\hat{r}}_{dh}$ and $\Delta i^{\hat{r}}_{qh}$ in a sampling period T_s can be expressed with HF injected voltage as

$$\begin{bmatrix} \Delta i^{\hat{r}}_{dh} \\ \Delta i^{\hat{r}}_{qh} \end{bmatrix} = \frac{T_s V_{\text{inj}}}{\sum L^2 - \Delta L^2} \begin{bmatrix} \sum L + \Delta L \cos(2\theta_{\text{err}}) \\ -\Delta L \sin(2\theta_{\text{err}}) \end{bmatrix} \cdot \text{clk}[k-1] \tag{22}$$

where $\sum L = (L_q + L_d)/2$. Therefore, the dc error signal $i_{q\text{·sig}}$ can be obtained as

$$i_{q\_\text{sig}} = \frac{\sum L^2 - \Delta L^2}{-2T_s V_{\text{inj}} \Delta L} \Delta i^{\hat{r}}_{qh} \cdot \text{clk}[k-1]. \tag{23}$$

However, current signal harmonics are generated due to non-idealities in the IPMSM and inverter nonlinearity. Consequently, the dc error signal $i_{q\text{·sig}}$ contains both position information and harmonic components, as expressed by

$$i_{q\_\text{sig}} = \theta_{\text{err}} + \sum_{i=1,2,3\ldots} A_{si}\sin(i\theta_e) + A_{ci}\cos(i\theta_e) \tag{24}$$

where A_{si} and A_{ci} are the amplitudes of the i^{th}-order harmonics. To adaptively suppress the harmonics without affecting the position observation, the ANF can be applied, as is illustrated in Fig. 2. The harmonics-suppressed estimation error is obtained in ANF as

$$\varepsilon_s = i_{q\_\text{sig}} - \sum_{i=1,2,3\ldots} \hat{A}_{si}\sin(i\hat{\theta}_e) + \hat{A}_{ci}\cos(i\hat{\theta}_e) \tag{25}$$

where the estimated harmonic amplitude $\hat{A}_{si}$ and $\hat{A}_{ci}$ can be calculated as

$$\begin{bmatrix} \hat{A}_{ci} \\ \hat{A}_{si} \end{bmatrix} = \int \left(\begin{bmatrix} \mu\varepsilon_s \cos(i\hat{\theta}_e) \\ \mu\varepsilon_s \sin(i\hat{\theta}_e) \end{bmatrix} \right) dt \tag{26}$$

thus the harmonics-suppressed saliency tracking can be realized as follows:

$$\hat{\theta}_e = \int [\varphi_p \varepsilon_s + \varphi_i \int (\varepsilon_s) dt] dt. \tag{27}$$

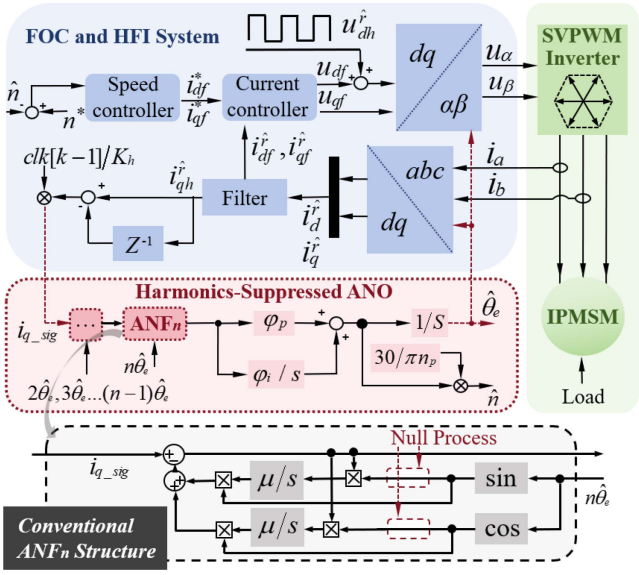

Fig. 2. Overall of the conventional ANO for the saliency tracking harmonics suppression.

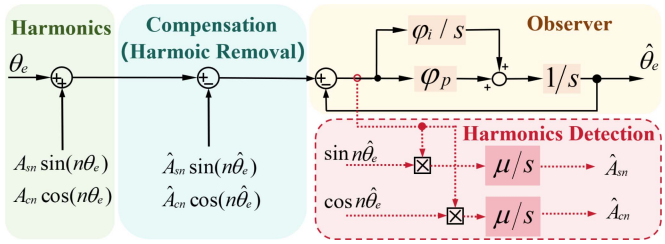

Fig. 3. Detailed schematic diagram of ANO and the inherent closed-loop nature in saliency tracking observer.

B. Convergence Boundary Analysis

The detailed schematic diagram of ANO is shown in Fig. 3, which contains both the harmonic section, the detection section and the compensation section. As only the estimation error information is available, the closed-loop nature in saliency tracking observer inherently exists. Hence, the phase misalignment between the harmonic detection section and harmonic compensation section which removes the detected harmonics is inevitably produced, leading to the divergence of the ANF.

The transfer function $G(s)$ from the compensation (which removes the detected harmonic signal) to the signal to be detected can be deduced as

$$G(s) = \frac{s^2}{s^2 + 2\xi\omega_n s + {\omega_n}^2}. \tag{28}$$

Hence, the amplitude-frequency $H(\omega)$ and phase-frequency characteristics $\phi(\omega)$ are calculated as

$$H(\omega) = \frac{\sqrt{\omega^4(\omega^2 - {\omega_n}^2)^2 + (2\xi\omega_n\omega^3)^2}}{(\omega^2 - {\omega_n}^2)^2 + 2\xi\omega_n\omega^2} \tag{29}$$

$$\phi(\omega) = \tan^{-1}\left(\frac{2\xi\omega_n\omega}{\omega^2 - {\omega_n}^2}\right). \tag{30}$$

For the n^{th}-order harmonics, the detected signal can be expressed as

$$\begin{aligned}\varepsilon_s &= \tilde{A}'_{sn}\sin(n\theta_e+\phi(n\omega_e))+\tilde{A}'_{cn}\cos(n\theta_e+\phi(n\omega_e))\\ &= H(n\omega_e)\{[\tilde{A}_{sn}\cos(\phi(n\omega_e))-\tilde{A}_{cn}\sin(\phi(n\omega_e))]\sin(n\theta_e)\\ &+[\tilde{A}_{sn}\sin(\phi(n\omega_e))+\tilde{A}_{cn}\cos(\phi(n\omega_e))]\cos(n\theta_e)\}\end{aligned} \tag{31}$$

where $\tilde{A}'_{sn}$ and $\tilde{A}'_{cn}$ are respectively obtained as

$$\begin{bmatrix}\tilde{A}'_{sn}\\ \tilde{A}'_{cn}\end{bmatrix} = H(n\omega_e)\begin{bmatrix}\tilde{A}_{sn}\\ \tilde{A}_{cn}\end{bmatrix} = H(n\omega_e)\begin{bmatrix}A_{sn}-\hat{A}_{sn}\\ A_{cn}-\hat{A}_{cn}\end{bmatrix} \tag{32}$$

where $\tilde{A}_{sn}$ and $\tilde{A}_{cn}$ are the error of suppression process. Hence, by substituting (31) into (26), the estimated amplitudes of the nth-order harmonic can be deduced as

$$\begin{aligned}\hat{A}_{sn} =\ &\mu H(n\omega_e)\int\{[\tilde{A}_{sn}\cos(\phi(n\omega_e))-\tilde{A}_{cn}\sin(\phi(n\omega_e))]\sin^2(n\theta_e)\\ &+[\tilde{A}_{sn}\sin(\phi(n\omega_e))+\tilde{A}_{cn}\cos(\phi(n\omega_e))]\cos(n\theta_e)\sin(n\theta_e)\}dt\end{aligned} \tag{33}$$

$$\begin{aligned}\hat{A}_{cn} =\ &\mu H(n\omega_e)\int\{[\tilde{A}_{sn}\sin(\phi(n\omega_e))+\tilde{A}_{cn}\cos(\phi(n\omega_e))]\cos^2(n\theta_e)\\ &+[\tilde{A}_{sn}\cos(\phi(n\omega_e))-\tilde{A}_{cn}\sin(\phi(n\omega_e))]\cos(n\theta_e)\sin(n\theta_e)\}dt\end{aligned} \tag{34}$$

the integrated value of the ac quantity in (33) and (34) equals to 0. Hence, the estimated amplitudes of nth-order harmonic can be calculated as

$$\begin{bmatrix}\hat{A}_{sn}\\ \hat{A}_{cn}\end{bmatrix} = \mu'\int\left(\begin{bmatrix}\tilde{A}_{sn}\cos(\phi(n\omega_e))-\tilde{A}_{cn}\sin(\phi(n\omega_e))\\ \tilde{A}_{sn}\sin(\phi(n\omega_e))+\tilde{A}_{cn}\cos(\phi(n\omega_e))\end{bmatrix}\right)dt \tag{35}$$

where μ' equals to $H(n\omega_e)\mu/2$. Therefore, the state equations of suppression error can be deduced as

$$p\tilde{A}_{sn} = -\mu'[\tilde{A}_{sn}\cos(\phi(n\omega_e))-\tilde{A}_{cn}\sin(\phi(n\omega_e))] \tag{36}$$

$$p\tilde{A}_{cn} = -\mu'[\tilde{A}_{sn}\sin(\phi(n\omega_e))+\tilde{A}_{cn}\cos(\phi(n\omega_e))]. \tag{37}$$

Hence, the sine and cosine components converge respectively when the following constraints are satisfied as:

$$\tilde{A}^2_{sn}\cos(\phi(n\omega_e))-\tilde{A}_{sn}\tilde{A}_{cn}\sin(\phi(n\omega_e))>0 \tag{38}$$

$$\tilde{A}_{cn}\tilde{A}_{sn}\sin(\phi(n\omega_e))+\tilde{A}^2_{cn}\cos(\phi(n\omega_e))>0. \tag{39}$$

To investigate the global convergence characteristic, the Lyapunov function can be established as

$$V_{lf} = \tilde{A}^2_{sn}+\tilde{A}^2_{cn} \tag{40}$$

by substituting (36) and (37), the derivative of the V_{lf} can be deduced as

$$\begin{aligned}pV_{lf} &= 2\tilde{A}_{sn}\cdot p\tilde{A}_{sn}+2\tilde{A}_{cn}\cdot p\tilde{A}_{cn}\\ &= -2\mu'(\tilde{A}^2_{sn}+\tilde{A}^2_{cn})\cos(\phi(n\omega_e)).\end{aligned} \tag{41}$$

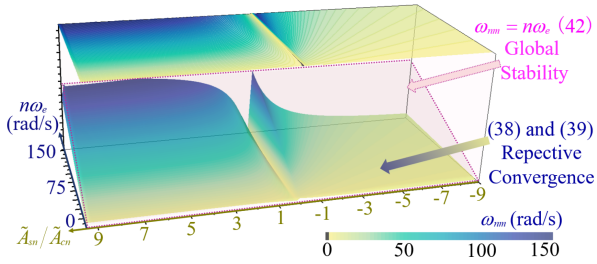

Fig. 4. Convergence boundary analysis of the harmonics-suppressed ANO.

Therefore, the global convergence of the harmonic suppression can be achieved when $\cos(\phi(n\omega_e))>0$. By utilizing (30), the global convergence boundary can be deduced as

$$n\omega_e > \omega_n. \tag{42}$$

Constraints (38) and (39) are graphically represented in Fig. 4 with solid curve. As is illustrated in (30), the phase misalignment resulting from closed-loop operation is strictly positive. Hence, increased phase lag components elevate the corresponding respective convergence boundary. Specifically, when the phase-lead component approaches infinitesimal levels, the respective convergence boundary approaches the global stability boundary, as clearly demonstrated in Fig. 4.

Therefore, although traditional ANF structures in closed-loop tracking observers provide adaptive harmonic suppression while maintaining position information integrity, two critical limitations emerge: pronounced divergence tendencies during low-speed operation (particularly affecting low-order harmonics) and progressively restricted convergence boundaries under elevated observation bandwidth.

IV. Proposed Full-Order Harmonics Suppressed DPS-ANO for High-Bandwidth Saliency Tracking

To solve the divergence risk in conventional ANF and to adaptively suppress the full-order harmonics under high-bandwidth observation without distorting the target position information, the structure of ANF is improved with the proposed dynamic phase synchronizer (DPS). The simplified illustration of comparison between conventional ANF and the proposed DPS-ANF is illustrated in Fig. 5. $h_{re\cdot disred}$ stands for the desired compensation signal. $h_{re\cdot InLoop}$ stands for the actual compensation signal in closed-loop. h_{de} is the detected harmonics and $h_{re\cdot app}$ stands for the calculated compensation signal applied to closed loop. The harmonics in the observation loop equals to $h_{de}+h_{re\cdot InLoop}$. For conventional ANF, when the applied signal $h_{re\cdot app}$ exactly equals to the inverse number of actual compensation signal in closed-loop $h_{re\cdot InLoop}$, the harmonics can be completely suppressed. However, due to the inevitable closed-loop nature in position observation, the difference is produced between $h_{re\cdot app}$ and $h_{re\cdot InLoop}$. Specifically, when frequency of harmonics is lower than the observation bandwidth, the phase shift between $h_{re\cdot app}$ and $h_{re\cdot InLoop}$ is larger than 90°. In such condition, the harmonics diverges to the opposite direction. In DPS-ANF, the destination of the proposed DPS is to make $h_{re\cdot InLoop}$ equals to $h_{re\cdot disred}$ ($-h_{de}$) by dynamically adjusting $h_{re\cdot app}$, thus counteracting the effect of closed-loop.

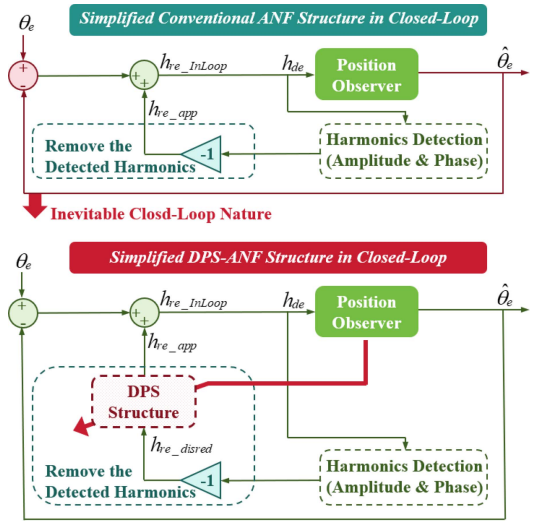

Fig. 5. Simplified illustration of comparison between conventional ANO and the proposed DPS-ANO.

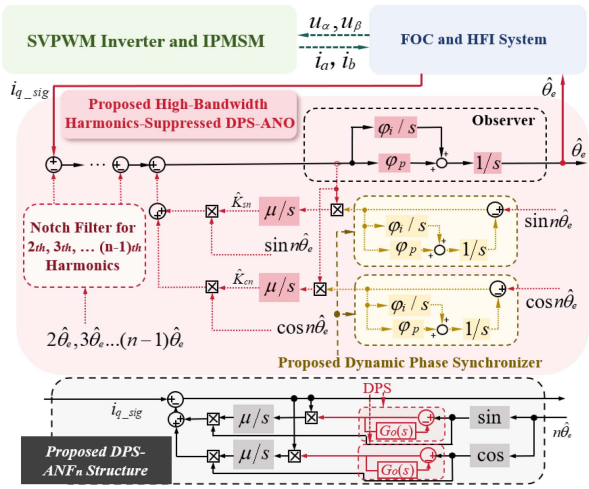

Fig. 6. Block diagram and detailed of the proposed high-bandwidth full-order harmonics suppressed DPS-ANO.

The details are illustrated in Fig. 6. The proposed DPS actively generates the phase shift between the detection and compensation section by cascading closed-loop structure, therefore the closed-loop effect can be counteracted. Besides, the parameters of the proposed DPS are varied depending on the observation bandwidth, thus realizing global convergence characteristic of full-order harmonics dynamically. $G_o(s)$ in Fig. 6 is the open-loop transfer function.

For the proposed DPS-ANO, the calculation of the estimated amplitude of the n^{th}-order harmonics $\hat{A}_{snd}$ and $\hat{A}_{cnd}$ can be expressed as follows:

$$\hat{A}_{snd} = \int \{\sin(n\theta_e + \phi(n\omega_e))[(\tilde{A}_{snd}\cos(\phi(n\omega_e)) - \tilde{A}_{cnd}\sin(\phi(n\omega_e)))\sin(n\theta_e) + (\tilde{A}_{snd}\sin(\phi(n\omega_e)) + \tilde{A}_{cnd}\cos(\phi(n\omega_e)))\cos(n\theta_e)]\}dt \cdot \mu H(n\omega_e)^2 \tag{43}$$

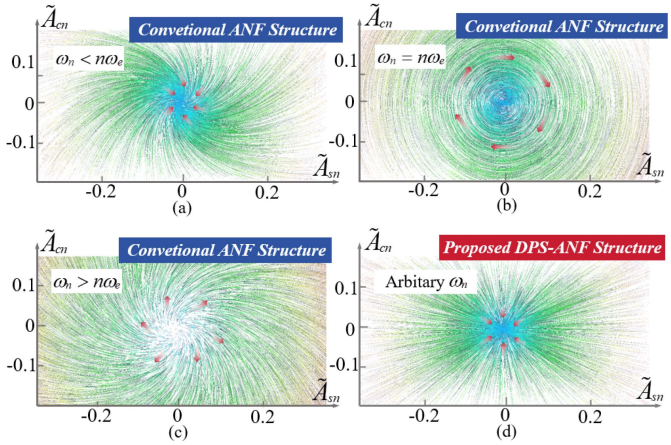

Fig. 7. Phase locus of the typical structure-based ANO and the proposed DPS-ANO under different observation bandwidth. (a) Typical structure-based ANO when $\omega_n < n\omega_e$. (b) Typical structure-based ANO when $\omega_n = n\omega_e$. (c) Typical structure-based ANO when $\omega_n > n\omega_e$. (d) Proposed DPS-ANO for arbitrary observation bandwidth.

$$\hat{A}_{cnd} = \int \{\cos(n\theta_e + \phi(n\omega_e))[(\tilde{A}_{snd}\cos(\phi(n\omega_e)) - \tilde{A}_{cnd}\sin(\phi(n\omega_e)))\sin(n\theta_e) + (\tilde{A}_{snd}\sin(\phi(n\omega_e)) + \tilde{A}_{cnd}\cos(\phi(n\omega_e)))\cos(n\theta_e)]\}dt \cdot \mu H(n\omega_e)^2 \tag{44}$$

where $\tilde{A}_{snd}$ and $\tilde{A}_{cnd}$ are defined as

$$\begin{bmatrix}\tilde{A}_{snd}\\ \tilde{A}_{cnd}\end{bmatrix} = \begin{bmatrix}A_{snd} - \hat{A}_{snd}\\ A_{cnd} - \hat{A}_{cnd}\end{bmatrix} \tag{45}$$

where A_{snd} and A_{cnd} are the actual amplitude of the n^{th}-order harmonics. Hence, by utilizing (43) and (44), the state equations of suppression error can be deduced as

$$p\begin{bmatrix}\tilde{A}_{snd}\\ \tilde{A}_{cnd}\end{bmatrix} = -\mu_d\begin{bmatrix}\tilde{A}_{snd}\\ \tilde{A}_{cnd}\end{bmatrix} \tag{46}$$

where μ_d equals to $\mu H(n\omega_e)^2/2$. To investigate the global convergence characteristic, the Lyapunov function for the proposed DPS-ANO can be established as

$$V_{lfd} = \tilde{A}_{snd}^2 + \tilde{A}_{cnd}^2 \tag{47}$$

hence, the product of V_{lfd} and its derivative can be calculated, which is inherently less than 0, as is expressed as

$$V_{lfd} \cdot pV_{lfd} = -\mu_d(\tilde{A}_{snd}^2 + \tilde{A}_{cnd}^2) < 0. \tag{48}$$

As shown in Fig. 7 [based on (36), (37) and (46)], the phase locus analysis reveals that the proposed DPS-ANO achieves enhanced convergence properties versus conventional ANO across all bandwidths, with particularly notable improvements in high-bandwidth scenarios. The inherent convergence of DPS-ANO allows full-order harmonic suppression without degrading saliency tracking bandwidth.

Besides, comparative discussion and performance analyses between the proposed DPS-ANO and existing filtering-based harmonic suppression methods ([28], [30], [31]) are conducted. Compared with typical transfer function-based methods which

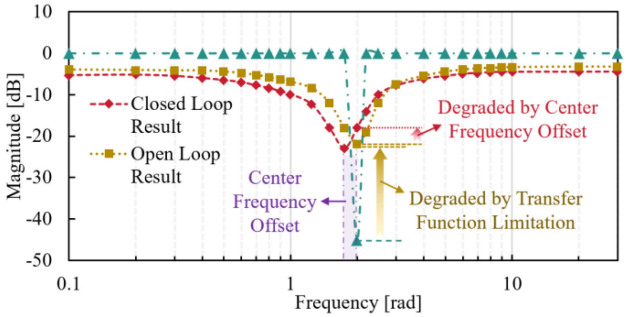

Fig. 8. Numerical result of filtering-based observer frequency response in [30], which shows the degraded low-order harmonic suppression performance due to transfer function limitation and center frequency offset.

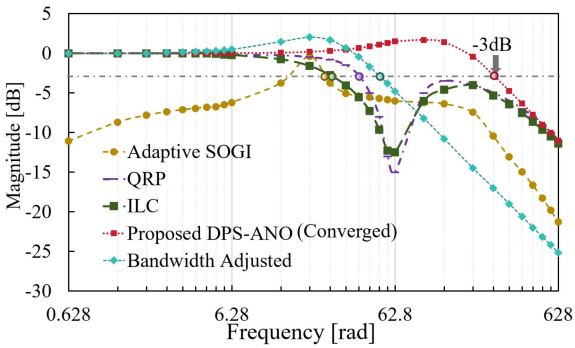

Fig. 9. Numerical result of frequency response and bandwidth comparison of different harmonic suppression methods.

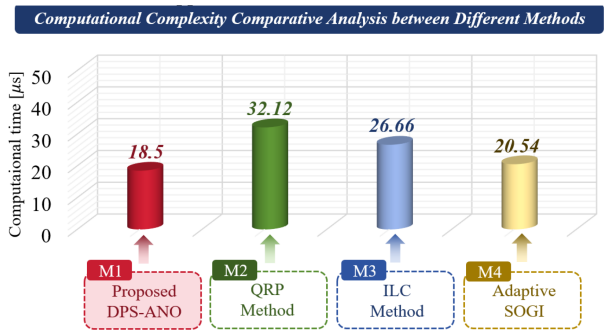

Fig. 10. Numerical result of computational complexity comparison of different harmonic suppression methods.

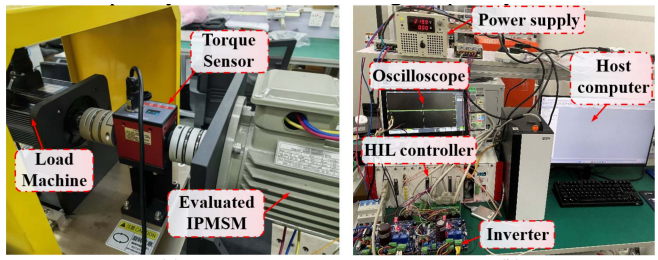

Fig. 11. Illustration for experimental platform. (a) Back-to-back machines and torque sensor. (b) Measurement, control, and driving devices.

ignore the close-loop effect, the DPS-ANO shows the enhanced full-order harmonic suppression performance. There are two key factors that could significantly degrade the low-order harmonic suppression performance in filtering-based methods: the limited gain for transfer function and the center frequency offset due to the closed-loop effect, as is illustrated in Fig. 8.

Additionally, the ANF-based method produces ignorable influence on the target signal observation when it converges, while the filtering-based methods inevitably degrades the fundamental signal observation. As is indicated in Fig. 9 that the frequency responses of existing filtering-based methods are significantly distorted. The bandwidth of the filtering-based observer can be reduced to less than 10.0% . Additionally, the observer bandwidth is also difficult to be tuned to the desired value by solely adjusting the PI controller parameters.

Besides, the computational complexity analysis is also conducted in cortex-M0 chip based on the time accumulation of basic operations. The comparison is illustrated in Fig. 10. It is indicated that, while the proposed DPS-ANO shows enhanced performance in harmonic suppression and target signal tracking, a computational complexity profile below that of existing harmonic suppression methods can also be achieved.

V. Experimental Results

Fig. 11 shows the photograph of the experimental platform. In Fig. 11(a), two back-to-back machines, including the evaluated IPMSM and the load machine, are illustrated. The measurement, control, and driving devices of the machines are shown in Fig. 11(b). The specifications of the evaluated IPMSM are given in Table I. In the experiments, the HF square wave injection is applied and the HF injection frequency is 5 kHz. The dc-bus voltage is 220 V and the dead-time of the inverter is 1μs. The control frequency and IGBT switching frequency are 10 kHz.

TABLE I
Specifications of the Evaluated IPMSM

Parameters	Values
Number of pole pairs	4
No-load PM flux linkage	0.625 Wb
Rated power	1.1 kW
Rated current	2.52 A
Winding resistance R_s	7.02 Ω
d-axis inductance L_d	36.72 mH
q-axis inductance L_q	83.95 mH

In Figs. 12 and 13, the convergence performances of the proposed typical structure-based ANO and the proposed DPS-ANO are illustrated, where the waveforms of the position and the estimated harmonic amplitudes are shown. Besides, different rotor speeds are applied to verify the failure of the basic structure-based ANO and the validity of the proposed convergence boundary. In the experiment, the bandwidth of 125 rad/s is adopted, by which different orders of harmonics can be reflected on the estimation error. As is indicated by Fig. 12(a) and (c), the typical structure-based ANO owns the capability of suppressing the harmonics with oscillation in high-speed ($\omega_e > \omega_n/n$) and fails to suppress the low-order harmonics

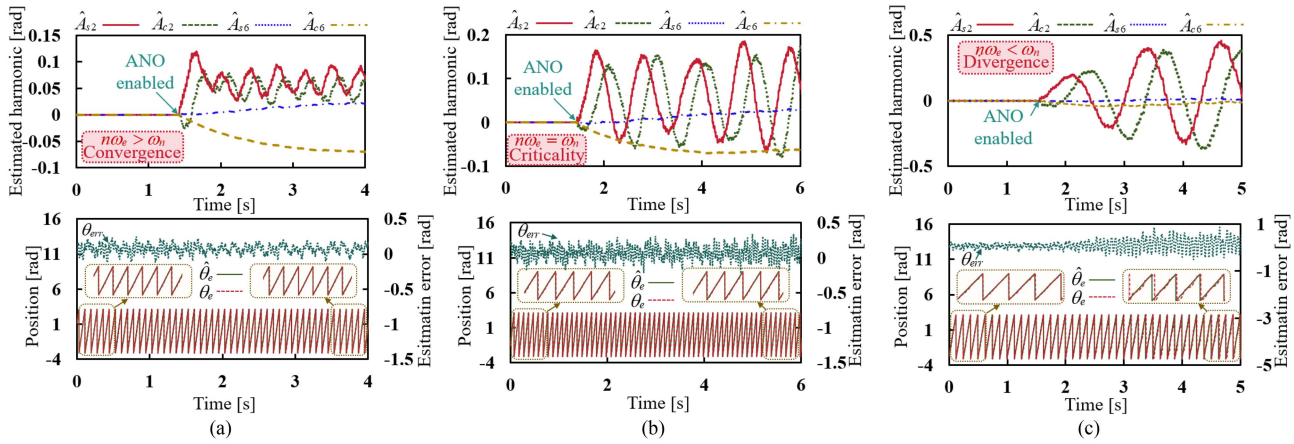

Fig. 12. Convergence performances of typical structure-based ANO under different speeds with the constant bandwidth. (a) Typical structure-based ANO under 180 r/min ($n\omega_e > \omega_n$). (b) Typical structure-based ANO under 150 r/min ($n\omega_e = \omega_n$). (c) Typical structure-based ANO under 120 r/min ($n\omega_e < \omega_n$).

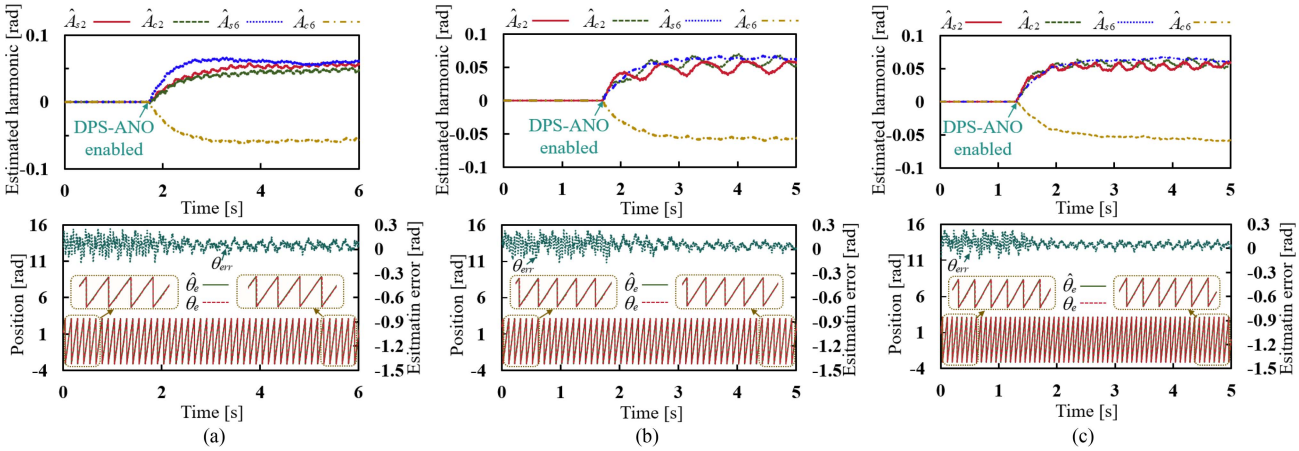

Fig. 13. Convergence performances of the proposed DPS-ANO under different speeds with the constant bandwidth. (a) DPS-ANO under 120 r/min ($n\omega_e < \omega_n$). (b) DPS-ANO under 150 r/min ($n\omega_e = \omega_n$). (c) DPS-ANO under 180 r/min ($n\omega_e > \omega_n$).

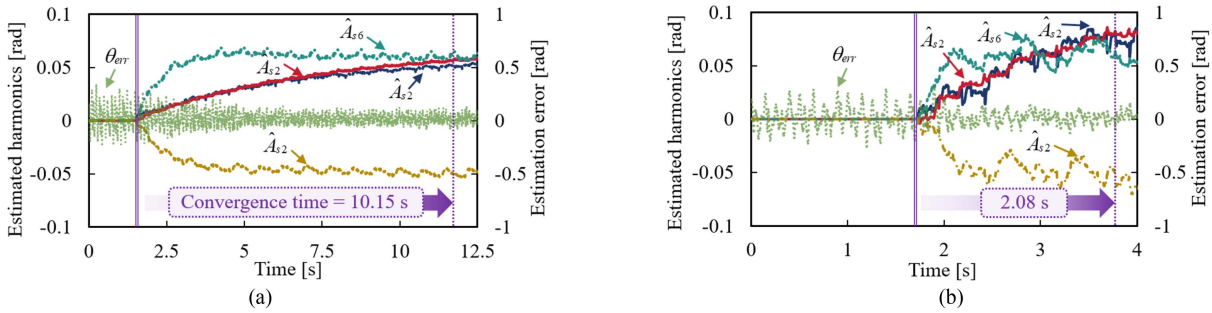

Fig. 14. Convergence characteristic of the proposed DPS-ANO with different adaption gains. (a) Adaption gain equals to 2. (b) Adaption gain equals to 10.

in low-speed ($\omega_e < \omega_n/n$). Additionally, the critical convergence condition is satisfied when $\omega_e = \omega_n/n$, as is illustrated in Fig. 12(b), which is consistent with the theoretical convergence boundary. In comparison, in the proposed DPS-ANO, the harmonics of different orders are inherently convergent with the oscillation less than 0.16 rad in different speeds, as is shown in Fig. 13. Additionally, for the identical adaption gain, enhanced dynamic adaption gain can be achieved, as is compared in Fig. 12(a) (converges over 1.7 s) and Fig. 13(a) (converges within 1.2 s).

Fig. 14 shows the practical tuning procedure of the adaption gain, which is reflected by the convergence characteristic of DPS-ANO. Adaptation gains of 2 and 10 are applied, respectively. A larger adaption gain will lead to faster convergence, while a smaller adaption gain could result in smoother and more stable convergence behavior. Moreover, the algorithm

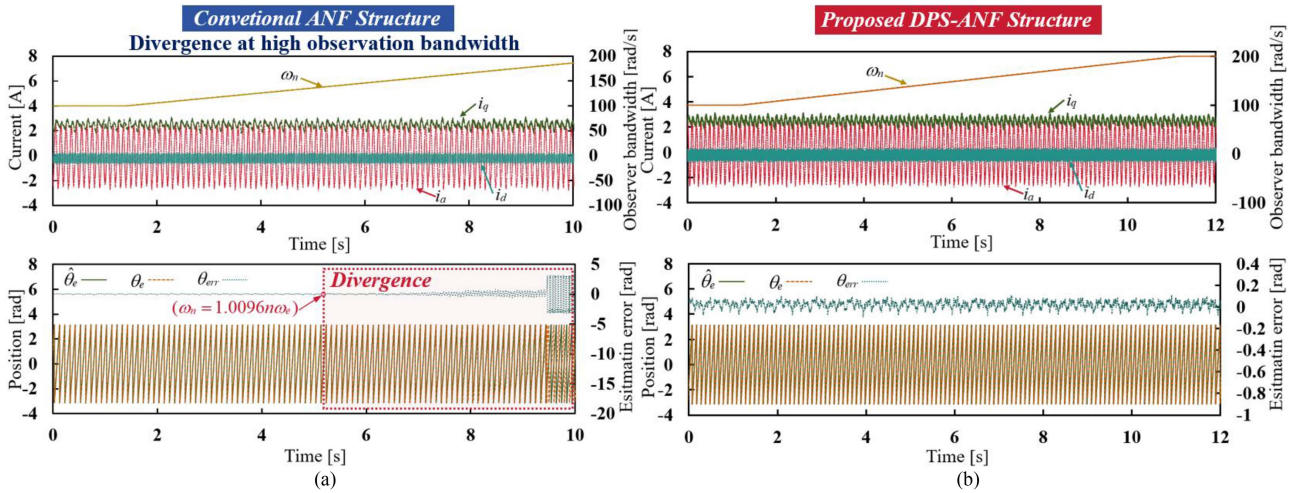

Fig. 15. Convergence performances of typical structure-based ANO and the proposed DPS-ANO under increasing bandwidth with the speed of 150 r/min. (a) Typical structure-based ANO. (b) Proposed DPS-ANO.

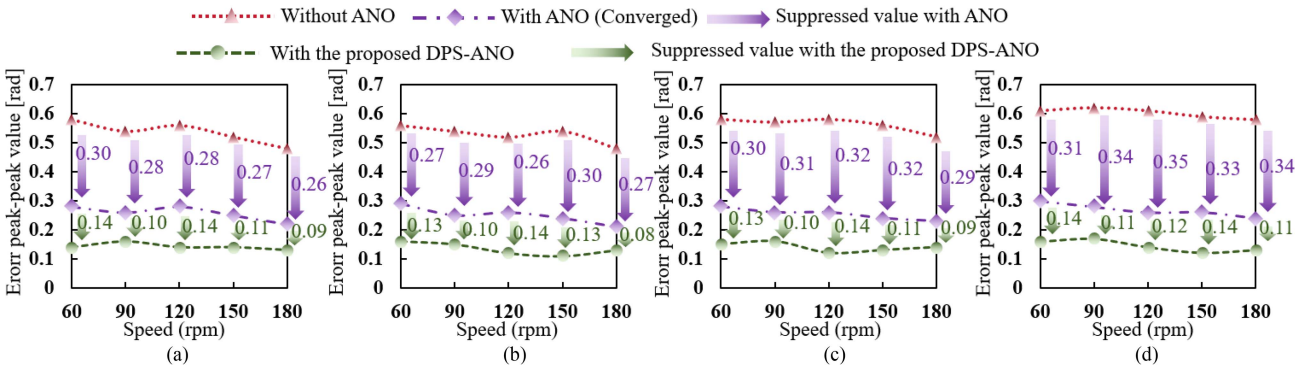

Fig. 16. Comparison of the estimation error peak-peak values versus speed under different loads with the conventional method, basic ANO-based method and the proposed DPS-ANO-based method. (a) No-load. (b) 0.3 p.u. (c) 0.6 p.u. (d) Rated load.

demonstrates strong robustness, as stable convergence is maintained across a wide range of adaptation gain values. In practice tuning procedure, the adaption gain can be determined by desired convergence rate.

Fig. 15 shows the convergence performances of the typical structure-based ANO and the proposed DPS-ANO under the increasing observation bandwidth. The results in Fig. 15(a) illustrates the failure of the basic structure-based ANO, where the conventional ANF becomes divergent when the observation bandwidth equals to 126.2 rad/s ($\omega_n = 1.0096n\omega_e$), validating the proposed convergence boundary. However, for the proposed DPS-ANO, the harmonic suppression performance will not be influenced by the variation of the observation bandwidth and the suppressed estimation error is inherently less than 0.09 rad, as is illustrated in Fig. 15(b).

Fig. 16 shows the experimental results of the estimation error peak-peak value reduction under different operation conditions. The comparison is conducted between the conventional HFI without harmonic suppression, the basic ANO when suppression process converges, and the proposed DPS-ANO. The results indicate that, without the harmonic suppression, the largest peak-peak value of the estimation error could reach 0.60 rad. While the basic ANO reduces it to less than 0.30 rad, achieving an error reduction of over 0.26 rad. By utilizing the proposed DPS-ANO, the peak-peak value of the estimation error can be reduced to 0.11 rad. The accuracy of position observation can be improved by 4.91 times.

Fig. 17 shows the estimation error waveforms comparison between the conventional method and the methods with different harmonic suppression methods. Conventional method is compared with the typical structure-based ANO and DPS-ANO in Fig. 17(a) and (b), respectively. The largest estimation error is reduced to 48% compared with conventional method when the typical structure-based ANO convergences. Besides, due to the enhanced convergence performance for low-order harmonics, the improved observation accuracy can be realized with the proposed DPS-ANO. The largest estimation error with the proposed DPS-ANO is 0.21 times of that with convention method.

The spectrum analysis of the estimation error is illustrated in Fig. 18. The spectrum in Fig. 18(a) shows the comparison between conventional observer and the typical structure-based

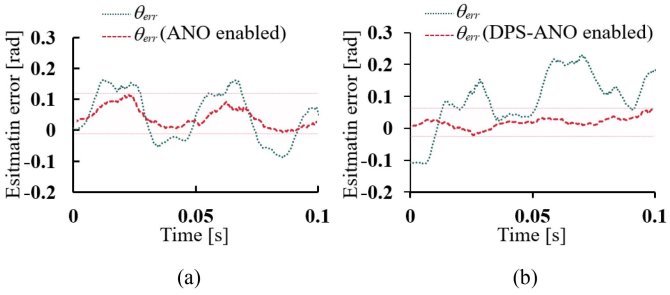

Fig. 17. Estimation error waveforms comparison between the conventional method and the methods with harmonic suppression. (a) Comparison between conventional observer and the typical structure-based ANO. (b) Comparison between conventional observer and the proposed DPS-ANO.

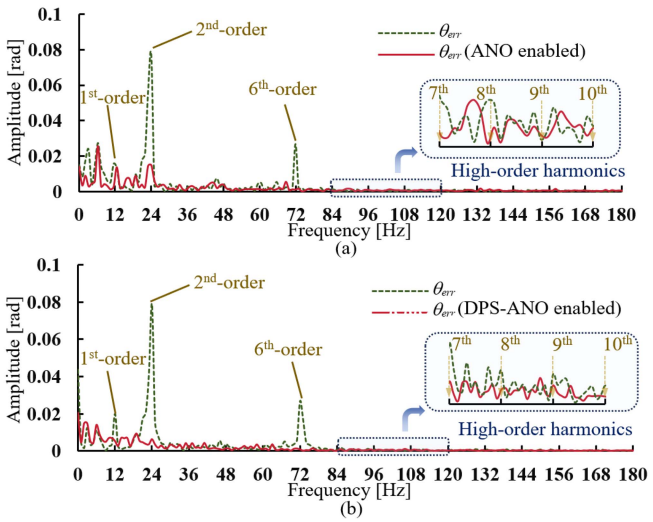

Fig. 18. Spectrum analysis of the estimation error. (a) Comparison between conventional observer and the typical structure-based ANO. (b) Comparison between conventional observer and the proposed DPS-ANO.

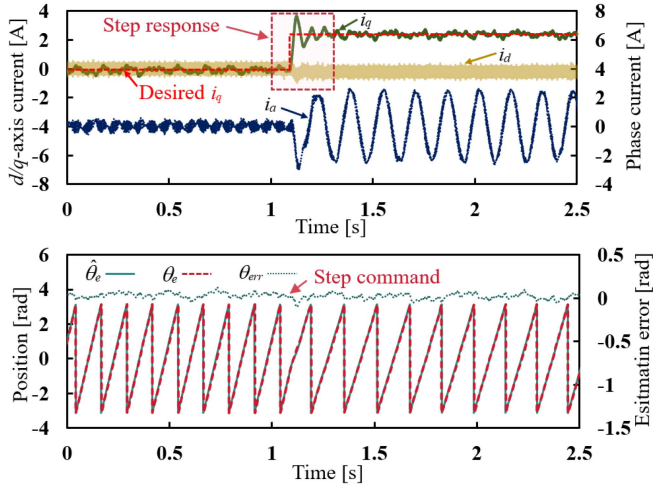

Fig. 19. Current waveforms and the performance of the proposed high-bandwidth DPS-ANO with step load (no-load to rated load) under 120 r/min.

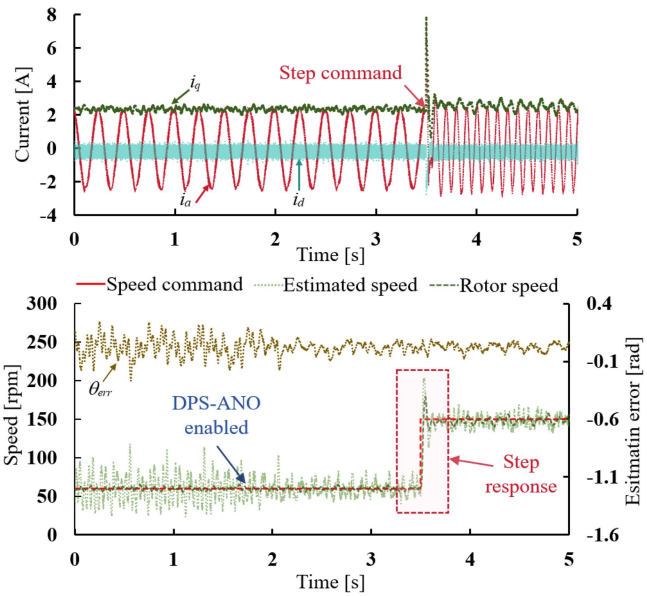

Fig. 20. Current waveforms and the performance of the proposed high-bandwidth DPS-ANO under step speed command (60 to 150 r/min) with rated load.

ANO. It is indicated that the dominant high-order harmonics (sixth-order produced from spatial harmonics of inductances and inverter nonideality) can be eliminated while the low-order harmonics (first-order and second-order produced from the current sampling offset and parameter asymmetry) are reduced ineffectively. Fig. 18(b) shows the performance of DPS-ANO, where full-order harmonics, including the dominating lower-order harmonics (first-order and second-order harmonics), can be effectively eliminated. Additionally, while the proposed DPS-ANF is capable of suppressing the higher order harmonics, they are too tiny to be measured in our experimental system.

In Figs. 19 and 20, the step load and step speed command are applied and the step response of position and speed tracking are illustrated, respectively, which verifies the high-bandwidth characteristic of the proposed harmonics-suppressed DPS-ANO. Specifically, under the step load transition from no-load to rated load at 120 r/min, as is illustrated in Fig. 19, the current exhibits rapid response to compensate the load disturbance with estimation error less than 0.09 rad, reflecting the high-bandwidth characteristics of both controller and the DPS-ANO. In Fig. 20, the high-bandwidth performance of the estimated speed is illustrated, whose error harmonics are suppressed and the estimation accuracy is enhanced when the proposed DPS-ANO is enabled and the step response is highlighted. When the step command (60 to 150 r/min) is performed, the rotor speed reaches the command value within 0.18 s, and the position estimation error of the proposed high-bandwidth DPS-ANO during the whole transient state is less than 0.10 rad.

Figs. 21–23 illustrate the performance comparison between the proposed DPS-ANO and existing high-performing harmonic suppression methods ([27], [28], [30], [31]). Additionally, the bandwidth adjusted strategy is also contained, which is the conventional method to reject the estimation error ripple.

Fig. 21 shows the estimation error spectrum comparison. It is indicated in the spectrum of conventional observer (without

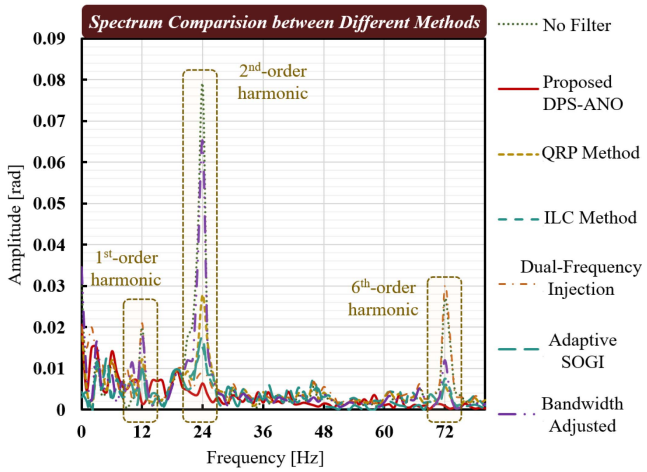

Fig. 21. Experimental estimation error spectrum comparison between the proposed DPS-ANO and different existing harmonic suppression methods.

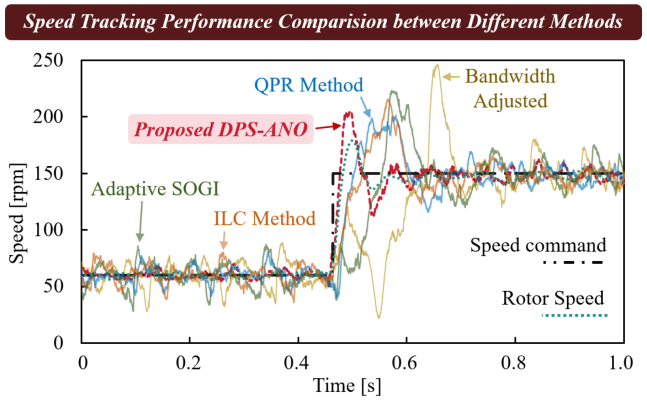

Fig. 22. Experimental dynamic tracking performance comparison under step speed command between the proposed DPS-ANO and different existing harmonic suppression methods.

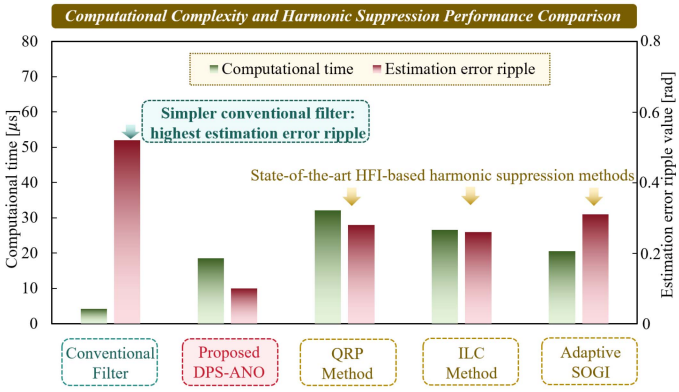

Fig. 23. Experimental computational time and harmonic suppression performance comparison.

additional filter) that the estimation error mainly contains the first-order, second-order and sixth-order harmonics. Conventionally, the estimation error ripple can be reduced with lower observation bandwidth. However, the suppression performance of the low-order harmonics is unsatisfactory in such method, as is illustrated in Fig. 21. Additionally, the dual-frequency injection-based method could reduce the second-order harmonic to 11.8% , while the first-order and the sixth-order harmonics can hardly be eliminated. Meanwhile, the adaptive SOGI, QRP method and ILC method exhibit degraded ability in suppressing low-order harmonics. In comparison, for the proposed DPS-ANO, the harmonic suppression performance for full-order harmonics is hardly degraded.

Fig. 22 illustrates the performance comparison of the speed tracking, which could indicate the target signal observation performance. In the experiment, the speed command from 60 to 150 r/min is applied. For the bandwidth adjusted method (by reducing the bandwidth of observer), the estimated speed rippled could reach 35.2% in steady state. The estimated speed ripple of existing harmonic suppression methods (adaptive SOGI, QRP method and ILC method) are 32.2% , 28.4% and 24.4% , respectively. In the proposed DPS-ANF, the estimated speed rippled is reduced to 15.7% . Besides, the speed estimation divergence happens under speed step command in bandwidth adjusted method. For existing harmonic suppression methods, the estimated speeds reach the rotor speed in 1.22 s, 1.13 s, and 1.12 s, respectively. In comparison, the proposed DPS-ANO demonstrates exceptional bandwidth capability and target signal observation performance. It rapidly converges to the target speed within 0.18 s and tracks it with higher fidelity.

Additionally, the computational time of each suppression observer is evaluated and compared experimentally in cortex-M0 chip. Compared with state-of-the-art filter-based methods, our method achieves significant improvement in harmonic suppression without introducing substantial additional computational burden, where the computational time can be reduced to 21.71 μs. Additionally, while the simpler conventional filter exhibits lower computational complexity (computational time equals to 4.2 μs), the harmonic suppression performance can be significantly degraded, where estimation error ripple is 5.2 times the proposed DPS-ANF.

VI. Conclusion

In this article, it is firstly revealed that due to the inherent closed-loop nature in saliency tracking, the misalignment between the compensation section and the detected section is inevitably produced, which limits the low-order harmonic suppression performance and causes the divergence in conventional ANF structure when $n\omega_e > \omega_n$. Subsequently, the structure of the ANF is improved with the proposed DPS, which shows the ability to counteract the closed-loop effect compared with conventional ANF structure, realizing full-order harmonic suppression and high-bandwidth saliency tracking concurrently. The bandwidth-constrained convergence boundary is deduced analytically based on the Lyapunov and the enhancements of the proposed DPS-ANO are verified with comparative experiments.

References

[1] L. Zhang, Y. Fan, C. Li, A. Nied, and M. Cheng, "Fault-tolerant sensorless control of a five-phase FTFSCW-IPM motor based on a wide-speed strong-robustness sliding mode observer," *IEEE Trans. Energy Convers.*, vol. 33, no. 1, pp. 87–95, Mar. 2018.

[2] C. Gong, Y. Hu, J. Gao, Y. Wang, and L. Yan, "An improved delaysuppressed sliding-mode observer for sensorless vector-controlled PMSM," *IEEE Trans. Ind. Electron.*, vol. 67, no. 7, pp. 5913–5923, Jul. 2020.
[3] I. Hwang, Y.-C. Kwon, and S.-K. Sul, "Enhanced dynamic operation of heavily saturated IPMSM in signal-injection sensorless control with ancillary reference frame," *IEEE Trans. Power Electron.*, vol. 38, no. 5, pp. 5726–5741, May 2023.
[4] Z. Lin, X. Li, Z. Wang, T. Shi, and C. Xia, "Minimization of additional high-frequency torque ripple for square-wave voltage injection IPMSM sensorless drives," *IEEE Trans. Power Electron.*, vol. 35, no. 12, pp. 13345–13355, Dec. 2020.
[5] G. Pu, H. Zhan, H. Yang, D. Wu, and D. Xu, "Additional average torque enhanced high efficiency sensorless method by using variable-axis high frequency current injection," *IEEE Trans. Ind. Electron.*, vol. 72, no. 9, pp. 8872–8882, Sep. 2025, doi:10.1109/TIE.2025.3539396.
[6] B. Shuang, Z. Q. Zhu, and X. Wu, "Improved cross-coupling effect compensation method for sensorless control of IPMSM with high frequency voltage injection," *IEEE Trans. Energy Convers.*, vol. 37, no. 1, pp. 347–358, Mar. 2022.
[7] D. Reigosa, P. Garcia, F. Briz, D. Raca, and R. D. Lorenz, "Modeling and adaptive decoupling of high-frequency resistance and temperature effects in carrier-based sensorless control of PM synchronous machines," *IEEE Trans. Ind. Appl.*, vol. 46, no. 1, pp. 139–149, Jan./Feb. 2010.
[8] Y. Park and S.-K. Sul, "A novel method utilizing trapezoidal voltage to compensate for inverter nonlinearity," *IEEE Trans. Power Electron.*, vol. 27, no. 12, pp. 4837–4846, Dec. 2012.
[9] L. M. Gong and Z. Q. Zhu, "A novel method for compensating inverter nonlinearity effects in carrier signal injection-based sensorless control from positive-sequence carrier current distortion," *IEEE Trans. Ind. Appl.*, vol. 47, no. 3, pp. 1283–1292, May/Jun. 2011.
[10] C.-E. Hwang, Y. Lee, and S.-K. Sul, "Analysis on the position estimation error in position-sensorless operation using pulsating square wave signal injection," in *Proc. IEEE Energy Convers. Congr. Expo.*, 2017, pp. 844–850.
[11] T. Hoshino and J. Itoh, "Output voltage correction for a voltage source type inverter of an induction motor drive," *IEEE Trans. Power Electron.*, vol. 25, no. 9, pp. 2440–2449, Sep. 2010.
[12] R. W. Hejny and R. D. Lorenz, "Evaluating the practical low-speed limits for back-EMF tracking-based sensorless speed control using drive stiffness as a key metric," *IEEE Trans. Ind. Appl.*, vol. 47, no. 3, pp. 1337–1343, May/Jun. 2011.
[13] S. Ye and X. Yao, "An enhanced SMO-based permanent-magnet synchronous machine sensorless drive scheme with current measurement error compensation," *IEEE J. Emerg. Sel. Topics Power Electron.*, vol. 9, no. 4, pp. 4407–4419, Aug. 2021.
[14] B. Wang, P. Du, Y. Yu, and D. Xu, "Sensorless PMSM harmonic suppression strategy based on PLL with embedded double quasi-proportional-resonant controllers," in *Proc. 2022 Int. Power Electron. Conf.*, 2022, pp. 372–377.
[15] W. Xu, Y. Jiang, C. Mu, and F. Blaabjerg, "Improved nonlinear flux observer-based second-order SOIFO for PMSM sensorless control," *IEEE Trans. Power Electron.*, vol. 34, no. 1, pp. 565–579, Jan. 2019.
[16] X. Wu et al., "Enhanced position sensorless control using bilinear recursive least squares adaptive filter for interior permanent magnet synchronous motor," *IEEE Trans. Power Electron.*, vol. 35, no. 1, pp. 681–698, Jan. 2020.
[17] Y. Yu, Y. Shao, F. Chai, and M. Cui, "Static-errorless position estimation for sensorless PMSM drives with enhanced robustness against the full-frequency domain disturbance," *IEEE Trans. Power Electron.*, vol. 37, no. 5, pp. 5884–5897, May 2022.
[18] S. Pranith, S. Kumar, B. Singh, and T. S. Bhatti, "Robust control system tuner and cascaded adaptive vectorial filter-based PV-battery system with a dual-loop ANF-PLL," *IEEE Trans. Ind. Electron.*, vol. 71, no. 12, pp. 16419–16429, Dec. 2024.
[19] P. Ray, P. K. Ray, B. P. Behera, and N. Singh, "An ANF cascaded normalized-Cf-soho based control approach and analysis of PV-UPQC under highly non-ideal grid and load conditions," *IEEE Trans. Ind. Appl.*, vol. 60, no. 5, pp. 7757–7770, Sep./Oct. 2024.
[20] P. Mohapatra, A. K. Panda, V. R. N. N, R. K. Lenka, and L. Senapati, "ANF-MAP based multipurpose control approach for single-stage grid-connected PV system," *IEEE Trans. Ind. Electron.*, vol. 71, no. 9, pp. 10898–10907, Sep. 2024.
[21] G. Wang, H. Zhan, G. Zhang, X. Gui, and D. Xu, "Adaptive compensation method of position estimation harmonic error for emf-based observer in sensorless IPMSM drives," *IEEE Trans. Power Electron.*, vol. 29, no. 6, pp. 3055–3064, Jun. 2014.
[22] Y. Ge, L. Yang, and X. Ma, "A harmonic compensation method for SPMSM sensorless control based on the orthogonal master-slave adaptive notch filter," *IEEE Trans. Power Electron.*, vol. 36, no. 10, pp. 11701–11711, Oct. 2021, doi: 10.1109/TPEL.2021.
[23] Q. Xu, S. Fang, and D. Huang, "Sensorless control for SPMSM using modified super-twisting observer considering resistance mismatch and VSI nonlinearity," *IEEE Trans. Transp. Electrific.*, vol. 11, no. 3, pp. 7389–7402, Jun. 2025.
[24] T. Wang, H. Zhang, Q. Gao, Z. Xu, J. Li, and C. Gerada, "Enhanced self-sensing capability of permanent-magnet synchronous machines: A novel saliency modulation rotor end approach," *IEEE Trans. Ind. Electron.*, vol. 64, no. 5, pp. 3548–3556, May 2017.
[25] N. Bianchi and S. Bolognani, "Influence of rotor geometry of an IPM motor on sensorless control feasibility," *IEEE Trans. Ind. Appl.*, vol. 43, no. 1, pp. 87–96, Jan./Feb. 2007.
[26] R. Raute, C. Caruana, C. S. Staines, J. Cilia, M. Sumner, and G. M. Asher, "Analysis and compensation of inverter nonlinearity effect on a sensorless PMSM drive at very low and zero speed operation," *IEEE Trans. Ind. Electron.*, vol. 57, no. 12, pp. 4065–4074, Dec. 2010.
[27] P. L. Xu and Z. Q. Zhu, "Carrier signal injection-based sensorless control for permanent-magnet synchronous machine drives considering machine parameter asymmetry," *IEEE Trans. Ind. Electron.*, vol. 63, no. 5, pp. 2813–2824, May 2016.
[28] X. Huang and C. Han, "Harmonic suppression for low speed sensorless control of SPMSM based on high voltage frequency pulsating signal injection," in *Proc. IEEE 3rd Inf. Technol., Netw., Electron. Automat. Control Conf.*, 2019, pp. 686–690.
[29] Y. Chen, X. Wu, Z. Zhu, and C. Liu, "Analysis and suppression of inductance asymmetry effect on high frequency signal injection sensorless control of permanent magnet synchronous machines," in *Proc. 25th Int. Conf. Elect. Machines Syst.*, 2022, pp. 1–6.
[30] G. Bi et al., "Adaptive quasi-proportional-resonant observer-based rotor position estimation for sensorless PMSM drives," *IEEE Trans. Power Electron.*, vol. 37, no. 12, pp. 15221–15233, Dec. 2022.
[31] G. Zhang et al., "Adaptive fourier ILC for mover position estimation error suppression for sensorless PMLSM drives," *IEEE J. Emerg. Sel. Topics Power Electron.*, vol. 13, no. 2, pp. 1627–1637, Apr. 2025.
[32] Y. Chen, X. Wu, Z. Q. Zhu, and C. Liu, "Improved pulsating signal injection sensorless control of dual three-phase IPMSMs with arbitrary inductance asymmetries in one set three-phase windings," *IEEE Trans. Ind. Appl.*, vol. 60, no. 4, pp. 6277–6290, Jul./Aug. 2024.

Guangyu Pu (Student Member, IEEE) was born in Sichuan, China, in 2001. He received the B.Eng. degree in electrical engineering from the Harbin Institute of Technology (Shenzhen), Shenzhen, China, where he is currently working toward the Ph.D. degree in electrical engineering.

His research interests include the design, analysis and control method of electrical machines, and robotic motion control.

Hanlin Zhan (Member, IEEE) received the B.Eng. and M.Sc. degrees in electrical engineering from Harbin Institute of Technology, Harbin, China, in 2012 and 2014, respectively, and the Ph.D. degree in electronics and electrical engineering from the University of Sheffield, Sheffield, U.K., in 2017.

He was as Staff Engineer with Corporate Research Center, Midea Group, from 2017 to 2020. In 2020, he was an Associate Professor with the Department of Robotics and Advanced Manufacturing, Harbin Institute of Technology (Shenzhen). Since 2024, he has been a Professor with the Department of Robotics and Advanced Manufacturing, Harbin Institute of Technology (Shenzhen), Shenzhen, China. His research interests include permanent magnet motor and drives for robotics, electric vehicle and home appliances, etc.

Wenzhi Liu was born in Hubei, China, in 2003. She received the B.Eng. degree in electrical engineering in 2025 from the Harbin Institute of Technology (Shenzhen), Shenzhen, China, where she is currently working toward the M.Sc. degree in electrical engineering.

Her research interests include the analysis and control of electrical machines.

Hui Yang (Senior Member, IEEE) received the B.Eng. degree in electrical engineering from Dalian University of Technology, Dalian, China, in 2011, and the Ph.D. degree in electrical engineering from Southeast University, Nanjing, China, in 2016.

He is currently a Full Professor with Nanjing University of Aeronautics and Astronautics, Nanjing, China. From 2014 to 2015, he was supported by China Scholarship Council through a one-year joint Ph.D. studentship with the University of Sheffield, Sheffield, U.K. From 2019 to 2020, he was a Post-Doctoral Fellow with the School of Electrical Engineering, The Hong Kong Polytechnic University, Hong Kong. He has authored or co-authored more than 120 IEEE TRANSACTIONS papers. His research interests include novel permanent-magnet machines and drives with particular reference to variable-flux machines for electric vehicles, robotics, and renewable energy applications.

Dr. Yang was a recipient of eight international conference best paper awards. He served as the Organizing Committee Chair of iSPEC 2021 and CIEEC 2022. He serves as an Associate Editor for IEEE TRANSACTIONS ON INDUSTRIAL ELECTRONICS and IEEE TRANSACTIONS ON ENERGY CONVERSION and an Editor of *World Electric Vehicle Journal*.

Lei Yang received the B.Eng. and M.Sc. degrees in electrical engineering from the Harbin Institute of Technology, Harbin, China, in 2015 and 2017, respectively, and the Ph.D. degree in electrical and electronic engineering from The University of Sheffield, Sheffield, U.K., in 2020.

Since 2020, he has been with the Midea Group Corporate Research Center, Foshan, China. His current research interests include permanent-magnet motors and drives for robotics, electric vehicle and home appliances.

Dianguo Xu (Fellow, IEEE) received the B.S. degree in control engineering from Harbin Engineering University, Harbin, China, in 1982, and the M.S. and the Ph.D. degrees in electrical engineering from Harbin Institute of Technology (HIT), Harbin, China, in 1984 and 1989, respectively.

In 1984, he was an Assistant Professor with the Department of Electrical Engineering, HIT. Since 1994, he has been a Professor with the Department of Electrical Engineering, HIT. He was the Dean of School of Electrical Engineering and Automation, HIT, from 2000 to 2010. He was the Vice President of HIT, from 2014 to 2020. He has authored or coauthored more than 600 technical papers. His research interests include motor drives, PMSM servo drives, renewable energy generation technology, and power quality mitigation, etc.

Dr. Xu is currently the co-EIC for IEEE TRANSACTIONS ON POWER ELECTRONICS, and an Associate Editor for IEEE TRANSACTIONS ON INDUSTRIAL ELECTRONICS and IEEE JOURNAL OF EMERGING AND SELECTED TOPICS IN POWER ELECTRONICS. He is currently the Chairman of IEEE Harbin Section.